Assessing the Ducting Phenomenon and its Potential Impact on GNSS Radio Occultation Refractivity Retrievals over the Northeast Pacific Ocean using Radiosondes and Global Reanalysis

Thomas E. Winning Jr.[1], Feiqin Xie[1] and Kevin J. Nelson[1,a]

[1] Texas A&M University – Corpus Christi, Corpus Christi, 78412, USA

[a] now at: Jet Propulsion Laboratory, California Institute of Technology, Pasadena, 91109, USA

Correspondence to: Thomas E. Winning Jr. (twinning@islander.tamucc.edu)

Abstract. In this study, high-resolution radiosondes from the MAGIC field campaign and ERA5 global reanalysis data are used to assess characteristics of the elevated ducting layer along a transect over the northeastern Pacific Ocean from Los Angeles, California to Honolulu, Hawaii. The planetary boundary layer (PBL) height (PBLH) increases as the strength of the refractivity gradient decreases westward along the transect. The thickness of the prevailing ducting layer remains remarkably consistent (~110 m) in the radiosonde data. On the other hand, the ERA5 reanalysis generally resolves the ducting features well, but underestimates the ducting height and strength, especially over the trade cumulus region near Hawaii. A simple two-step end-to-end simulation is used to evaluate the impact of the elevated ducting layer on RO refractivity retrievals. A systematic negative refractivity bias (*N*-bias) below the ducting layer is observed throughout the transect, peaking (−5.42%) slightly below the PBLH, and gradually decreasing towards the surface (−0.5%). The *N*-bias shows strong positive correlation with the ducting strength. The ERA5 data underestimate the *N*-bias with the magnitude of the underestimation increasing westward along the transect.

1 Introduction

The troposphere, where most weather occurs, consists of two main layers: the planetary boundary layer (PBL) and the free atmosphere (FA) (Garratt, 1994). The PBL characteristics change frequently on both spatial and temporal scales and the PBL height (PBLH) can impact the exchange of heat, momentum, and particulate matter with the FA, making it a critical factor in global energy balances and water cycling (Stull 1988; Ramanathan et al. 1989; Klein and Hartmann 1993). Regular PBL observations are mainly limited to in-situ measurements from surface stations and radiosondes. However, spatially and temporally dense in-situ PBL observations are typically only available from field campaigns such as the Boundary Layer Experiment 1996 (BLX96, Stull et al. 1997), the Variability of the American Monsoon Systems (VAMOS) Ocean-Cloud-Atmosphere-Land Study Regional Experiment (VOCALS-REx, Wood et al. 2011), and the Marine Atmospheric Radiation Measurement (ARM) Global Energy and Water Experiment (GEWEX) Cloud System Studies (GCSS) Pacific Cross Section Intercomparison (GPCI) Investigation of Clouds (MAGIC, Zhou et al. 2015). Satellite observations of the PBL are also limited due to signal attenuation of the conventional infrared sounder in the lower troposphere and the low vertical resolution of microwave sounding instruments. Additionally, while the depth of the PBLH can vary from a couple hundred meters to a few kilometers (Ao et al. 2012; von Engeln and Teixeira 2013), the transition layer from the PBL to the FA is typically on the order of tens to hundreds of meters thick (Maddy and Barnet 2008), rendering PBL sensing from the low vertical resolution passive infrared and microwave sounders ineffective.

On the other hand, Global Navigation Satellite System (GNSS) radio occultation (RO) provides global atmospheric soundings with a vertical resolution of approximately 100 m in the lower troposphere under all weather conditions (Kursinski et al., 1997, 2000; Gorbunov et al., 2004). Some of the recent major GNSS RO missions are the Formosat-3/Constellation Observing System for Meteorology, Ionosphere, and Climate (COSMIC), later referred to as COSMIC-1 (Anthes et al. 2008), and its follow-on mission COSMIC-2 (Schreiner et al. 2020). Numerous studies have documented the high value of GNSS RO for profiling the PBL and determining the PBLH (Ao et al. 2008; Xie et al. 2008; Basha and Ratnam 2009; Guo et al. 2011; Ao et al. 2012; Ho et al. 2015; Winning et al. 2017; Nelson et al. 2021).

60 The advancement of the GNSS RO technique with open-loop tracking (Ao et al., 2003; Beyerle et
61 al., 2003; Sokolovskiy et al., 2006) along with the implementation of radio-holographic retrieval
62 algorithms (Gorbunov, 2002; Jensen et al., 2003; Jensen et al., 2004) have led to much-improved
63 PBL sounding quality. However, probing the marine PBL remains challenging, as systematic
64 negative biases are frequently seen in RO refractivity retrievals (Xie et al. 2010; Feng et al. 2020).
65 One major cause of refractivity bias (hereafter N-bias) is the RO retrieval error due to elevated
66 atmospheric ducting often seen near the PBLH (Sokolovskiy 2003; Ao et al. 2003; Xie et al., 2006;
67 Ao et al., 2007). This elevated ducting is found primarily over the subtropical eastern oceans (von
68 Englen et al., 2003; Lopez, 2009; Feng et al., 2020), and the horizontal extent of ducting in these
69 regions can be on the order of thousands of kilometers (Xie et al. 2010; Winning et al. 2017). In
70 the presence of ducting, the vertical refractivity gradient exceeds the critical refraction threshold
71 for L-band frequencies (i.e., $dN/dz \leq -157$ N-units km^{-1}). The steep negative refractivity gradient
72 is often observed in the vicinity of the PBLH, which is typically caused by an atmospheric
73 temperature inversion, a sharp decrease in moisture, or a combination of both. When ducting is
74 present, the Abel inversion (e.g., Fjeldbo et al., 1971) in the standard RO retrieval process
75 encounters a non-unique inversion problem due to a singularity in the bending angle, resulting in
76 large, systematic underestimation of refractivity (N) below the ducting layer (Ao et al., 2003;
77 Sokolovskiy, 2003; Xie et al. 2006). The large uncertainty in RO refractivity coupled with the
78 singularity in bending angle hinders assimilation of RO observations into numerical weather
79 models, resulting in the rejection of a significant percentage of RO measurements inside the PBL
80 (Healy, 2001).
81 To comprehensively assess the potential impact of ducting on GNSS RO retrievals, we begin by
82 constructing a detailed ground truth of PBL ducting statistics. This is derived from an extensive
83 set of high-resolution radiosonde data over the northeastern Pacific Ocean, a region known for
84 prevailing ducting conditions. Subsequently, we conduct a simulation study using the radiosonde
85 data to evaluate the N-biases caused by varying ducting characteristics. Section 2 provides details
86 of the two data sets used for this study: high-resolution radiosondes over the northeastern Pacific
87 Ocean and the colocated ECMWF Reanalysis version 5 (ERA5, Hersbach et al. 2020) profiles.
88 Additionally, we discuss the colocation criteria and the detection method for ducting layer and the
89 corresponding PBLH. Section 3 presents the ducting statistics for key variables, such as ducting
90 height, PBLH, minimum refractivity gradient, and sharpness parameter. The characteristics of

91 ducting including the thickness and strength along the cross-section are also shown. Furthermore,
92 we evaluate the ducting-induced *N*-bias in GNSS RO refractivity retrievals by carrying out a two-
93 step end-to-end simulation. Section 4 summarizes the findings and discusses the direction of future
94 research.

95 **2   Data and methods**

96 **2.1 MAGIC radiosonde and colocated ERA5 data**

97 A collection of high-resolution radiosondes from the Marine Atmospheric Radiation Measurement
98 (ARM) GCSS Pacific Cross Section Intercomparison (GPCI) Investigation of Clouds (MAGIC)
99 are utilized as the primary data set in this analysis (Zhou et al. 2015; Lewis 2016). The MAGIC
100 field campaign took place from 26 September 2012 to 2 October 2013 as part of the U.S
101 Department of Energy ARM Program Mobile Facility 2 (AMF2) aboard the Horizon Lines
102 container ship, *Spirit*, which completed 20 round trip passes between Los Angeles, California and
103 Honolulu, Hawaii during the yearlong data collection period (Painemal et al., 2015; Zhou, 2015).
104 During each transit, radiosondes were launched at 6-hour intervals from the beginning of the
105 program through the end of June 2013; the observation frequency increased to every 3 hours from
106 July 2013 through the end of the campaign (Zhou et al., 2015). A total of 583 MAGIC radiosonde
107 profiles were collected during the field campaign (Zhou et al., 2015), all with a vertical sampling
108 frequency of 0.5 Hz (2 seconds), which provides an average vertical resolution of ~8 m below 3
109 km, but varies due to local vertical motion.
110 Use of this data set serves multiple benefits. First, the northeast Pacific transitions from a shallow
111 stratocumulus-topped PBL to a deeper, trade-cumulus boundary layer regime along the GPCI
112 transect shown in Figure 1 (Garratt, 1994). Second, the large number of observations over a 12-
113 month time frame provides high temporal (diurnal- and seasonal-scale) and spatial profiling of the
114 PBL along the GPCI transect (Fig. 1). Finally, ducting is prevalent throughout the domain over
115 which the observations were captured creating an opportunity to perform an analysis over a natural
116 cross-section of X (zonal) and Z (vertical) dimensions.
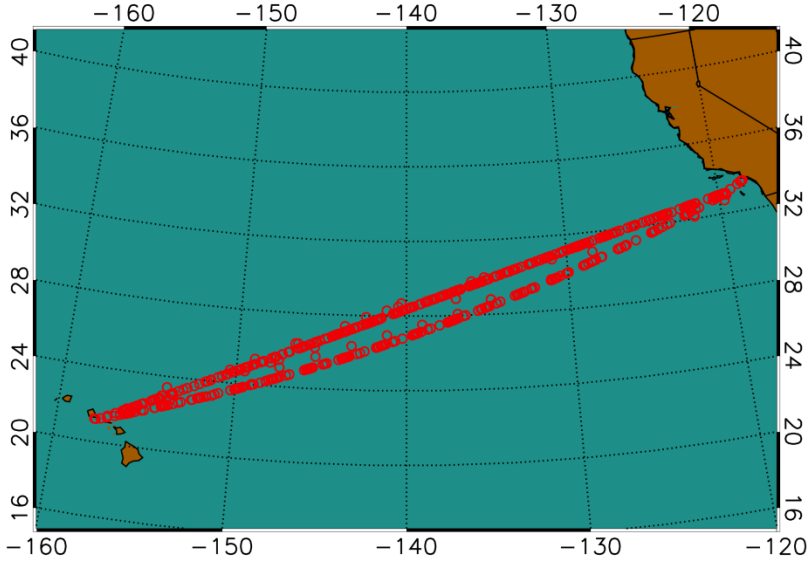
117
118 **Figure 1: Location of radiosonde observations from the MAGIC field campaign October 2012–September 2013.**

119

120   The radiosonde profiles are colocated with ERA5 model profiles for this analysis. The ERA5 data

121   have a horizontal resolution of 0.25°x0.25°, 137 non-equidistant vertical model levels from the

122   surface to 0.01 hPa, and 1-hour temporal resolution. The model level density decreases with height:

123   on average, there are 19 model levels below 1 km (10 –100 m resolution), which reduces to 8

124   levels between 1 and 2 km (100 – 160 m resolution), and further reduces to 5 levels between 2 and

125   3 km (160-200 m resolution). Each MAGIC radiosonde profile was colocated with the nearest

126   ERA5 grid point that is within 1.5 hours of the closest 3-hourly model profile.

127 **2.2 PBLH detection with the minimum gradient method**

128   At GNSS L-band frequencies, the atmospheric refractivity (N in N-units) is derived from the

129   refractive index n, where $N = (n-1) \times 10^6$ and, in the neutral atmosphere (Kursinski et al., 1997),

130   is a function of the atmospheric pressure (P in mb), temperature (T in K), and partial pressure of

131   water vapor (P_w in mb) as seen in Eq. (1) from Smith and Weintraub (1953).

132     $N = 77.6\frac{P}{T} + 3.73 \times 10^5 \frac{P_w}{T^2},$ (1)

133   Over the subtropical eastern oceans, a sharp decrease in moisture is often associated with a strong

134   temperature inversion marking a clear transition from the PBL to the FA. The distinct decrease in

135   moisture and the temperature inversion leads to a sharp negative refractivity gradient which can

136   be precisely detected from GNSS RO. Numerous studies have implemented the simple gradient

137   method to detect the PBLH, i.e., the height of the minimum refractivity gradient (Xie et al., 2006;

138   Seidel et al., 2010; Ao et al., 2012). To assess the robustness of the PBLH detection with the

139   gradient method, Ao et al. (2012) introduced the sharpness parameter ($\widetilde{N}'$) to measure the relative

140   magnitude of the minimum gradient, which is defined as the ratio of the minimum vertical

141   refractivity gradient (N'_{min}) to the root mean square (N'_{RMS}) of the refractivity gradient profile from

142   surface to 5 km as follows.

143 $$\widetilde{N}' \equiv - \frac{N'_{min}}{N'_{RMS}}, \tag{2}$$

144   In this study, the MAGIC radiosonde refractivity profiles were first interpolated to a uniform 10

145   m vertical grid and then smoothed by a 100 m boxcar window to reduce the noise in the gradient

146   profile resulting from the high sampling rate. Moreover, the 100 m smoothed radiosonde will be

147   more consistent with the vertical resolution of GNSS RO measurements (e.g., Gorbunov et al.,

148   2004). Colocated ERA5 data were also vertically interpolated to the same 10 m grid but not

149   smoothed as these data do not contain the inherent noise as the radiosonde observations. In the

150   case of both data sets, quadratic interpolation is used to translate the refractivity profiles from their

151   native height values to a uniform height. Finally, as the elevated ducting layer is the focus of this

152   study, the lowest 0.3 km above mean-sea-level of the *N*-profile are excluded (e.g., Xie et al., 2012).

153   Subsequently, the height of the minimum refractivity gradient (within 0.3 km and 5 km) will be

154   identified as the PBLH.

155   **2.3 Ducting layers**

156   The refractivity gradient profile is calculated by differentiating the 10 m interpolated refractivity

157   profile with respect to height. When the vertical refractivity gradient is less than the critical

158   refraction threshold for radio waves (dN/d$z < -157.0$ *N*-units km^{-1}), ducting occurs (Sokolovskiy,

159   2003). A ducting layer is identified as any interval of continuous points with a vertical refractivity

160   gradient equal to or less than the critical refraction threshold. Instances of multiple ducting layers

161   occurring within a profile are present for both the MAGIC (31.5%) and ERA5 (6.7%) data sets. In

162   this study, we only recognize one dominant "ducting layer" in each profile where the minimum

163   vertical gradient is located. The ducting layer thickness (Δh) is defined as the interval between the

164   top and bottom of the ducting layer where the refractivity gradients reach critical refraction.

165   Similarly, the strength of each ducting layer (ΔN) is defined as the refractivity difference between

166 the bottom and top of the ducting layer. The ducting layer height is defined as the height of the top

167 of the ducting layer (Ao, 2007), which is generally slightly above the PBLH.

168 Figure 2 shows vertical profiles of refractivity (*N* in da*N*-units), temperature (*T* in ˚C), and specific

169 humidity (*q* in g/kg) along with their respective vertical gradients (d*N*/dz, d*T*/dz, and d*q*/dz) from

170 a representative MAGIC radiosonde (Fig. 2a,b) case located at (23.69˚, −150.02˚), and its

171 colocated ERA5 (Fig. 2c,d) profile at (23.75˚, −150.00˚). The PBLH of the radiosonde (2.10 km)

172 is almost identical to the colocated ERA5 (2.14 km) and the "dominant" ducting layer near the

173 PBLH demonstrates similar thickness. However, a second, weaker ducting layer seen in the

174 radiosonde above the PBLH was not captured by the ERA5. It should be noted that the weak "saw

175 tooth-like" gradients seen above the minimum in the ERA5 refractivity gradient (Fig. 2d) are a

176 result of the vertical derivative being calculated from the interpolated ERA5 refractivity profile.

177 When interpolating the relatively coarse vertical resolution ERA5 profile (up to 200 m in the

178 lowest 3 km) into 10 m vertical sampling, the higher-order interpolation could lead to fine structure

179 in the first order derivative. However, these minor gradients ~~do not~~only marginally affect the

180 estimates of minimum gradient and associated heights from ERA5 and is most often overshadowed

181 by the PBLH gradient.

182
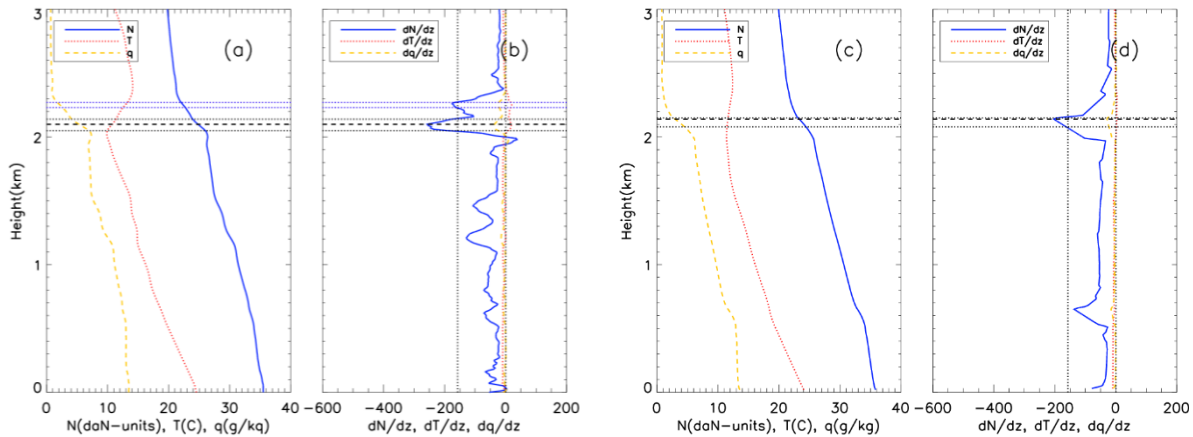
Figure 2: Vertical profiles of refractivity (*N* in da*N*-units, solid blue), temperature (*T* in ˚C, dotted red) and specific humidity (*q* in g kg⁻¹, dashed gold) for (a) radiosonde at (23.69˚, -150.02˚) launched at 2013-10-02, 05:30 UTC, and (c) colocated ERA5 at (23.75˚, -150.00˚); and associated gradient profiles for radiosonde (b) and ERA5 (d). The horizontal dashed line highlights the height of the minimum gradient, i.e., PBLH. The paired horizontal dotted lines represent the bottom and top of any ducting layers.

2.4 Evaluation of GNSS RO *N*-bias resulting from ducting

189 In order to estimate the systematic negative *N*-bias in GNSS RO observations in the presence of

190 ducting, we use an end-to-end simulation on the radiosonde and ERA5 refractivity profiles. The

7

191 simulation consists of a two-step process adapted from Xie et al. (2006). The first step is to
192 simulate the 1-dimensional GNSS RO bending angle as a function of impact parameter (i.e., the
193 product of refractive index and the radius of the Earth's curvature) by forward Abel integration of
194 an input refractivity profile assuming a spherically symmetric atmosphere (Fjeldbo and Eshleman,
195 1968; Eshleman, 1973; Sokolovskiy, 2001). The second step is to simulate the spaceborne GNSS
196 RO refractivity retrieval by applying the Abel inversion on the simulated bending angle from step
197 one. In the absence of ducting, the impact parameter increases monotonically with height, allowing
198 a unique solution to the inverse Abel retrieval that is the same as the original refractivity profile
199 input. However, in the presence of an elevated ducting layer, the Abel retrieval systematically
200 underestimates the refractivity profile due to the non-unique Abel inversion problem resulting
201 from the singularity in bending angle across the ducting layer (Sokolovskiy 2003; Xie et al., 2006).
202 It should be noted that after the 100 m vertical smoothing on radiosonde (no smoothing is
203 performed on ERA5) profiles as described in section 2.2, an additional 50 m vertical smoothing
204 has been applied to the simulated bending angle profiles of both radiosonde and ERA5 data sets
205 to alleviate the challenge of integration through the very sharp bending angle resulting from
206 ducting in the inverse Abel integration procedure (Feng et al., 2020).
207 Figure 3 shows the end-to-end simulation results for the same radiosonde (a–d) and the colocated
208 ERA5 (e–h) cases from Fig. 2. Figures 3a and 3e show refractivity profiles from the radiosonde
209 (N_{MAGIC}) and the colocated ERA5 (N_{ERA5}) data as well as their corresponding Abel refractivity
210 retrievals (N_{Abel}). The refractivity gradients are shown in Figures 3c and 3g. The derived PBLH is
211 marked by a horizontal dotted line in the refractivity/height space. The peak bending angles in
212 Figures 3d and 3h are consistent with the corresponding sharp refractivity gradient. Figure 3b
213 shows the fractional *N*-bias between the simulated Abel retrieved RO refractivity profile and the
214 radiosonde, whereas Figure 3f shows the same for the ERA5 profile. Considering the significant
215 spatial and temporal variations of ducting height along the transect, each *N*-bias profile is displayed
216 as a function of an adjusted height, which is the height minus the corresponding PBLH for the
217 purposes of profile intercomparison. For example, the zero-adjusted height refers to the PBLH for
218 each individual profile. The systematic negative *N*-bias is shown below the ducting layer marked
219 by the PBLH in both cases, with the biases decreasing at lower altitude, the largest magnitude bias
220 (−5% for radiosonde; −2.5% for ERA5) close to the ducting height and a minimum magnitude
221 approaching zero near the surface.
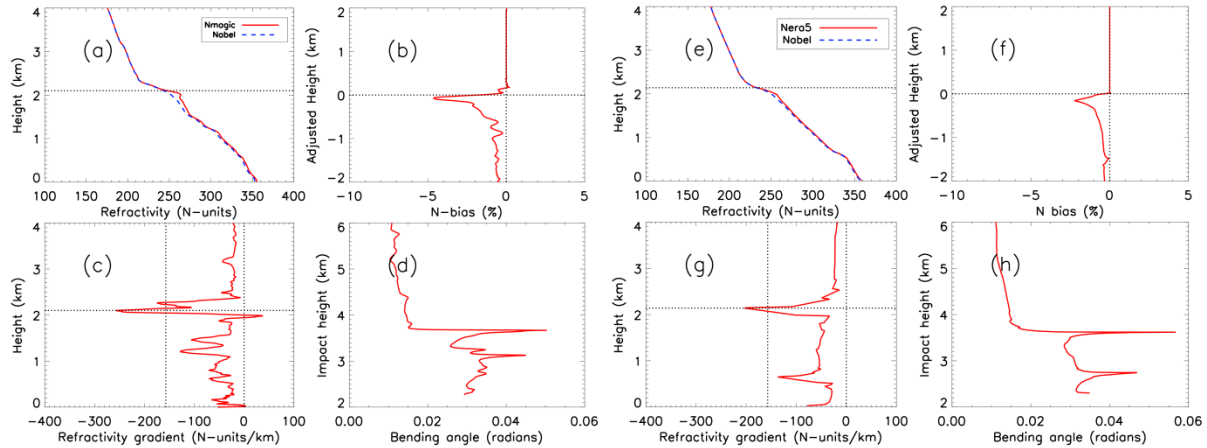
Figure 3: End-to-end simulation results for a MAGIC radiosonde launched at 0530 UTC on 20131002 showing: (a) N_{MAGIC}
(solid red) and N_{Abel} **(blue dashed) from surface to 4 km; (b) PBLH adjusted** N**-bias; (c) vertical refractivity gradient and**
(d) bending angle vs. impact parameter. Panels e-h show end-to-end simulation results for the colocated ERA5 profile.

## 3   Analysis

Quality control for radiosonde (and colocated ERA5) profiles was based on five key criteria. First, a total of 19 radiosonde and 24 ERA5 profiles near the southern California coast were removed due to their positions east of −120˚ or anomalously high PBL (PBLH > 3.0 km) with no distinct minimum gradient. The remaining profiles in the easternmost portion of the domain were too few in number to calculate meaningful statistics. Second, any profile lacking critical refraction (i.e. $dN/dz < -157$ N-units km^{-1}) points was excluded from the analysis which resulted in the removal of 47 radiosonde and 176 ERA5 profiles. Third, an anomalously noisy bending angle profile could result in errors in Abel refractivity retrieval and cause positive N-bias. Therefore, the profiles with N-bias greater than +0.5% are excluded resulting in the removal of 61 MAGIC profiles and 16 ERA5 profiles. Fourth, the profiles with only surface ducting, i.e., below 300 m threshold, are discarded. Finally, 25 radiosonde profiles and 2 ERA5 profiles were removed due to the Abel retrieval failure. After implementing all quality control measures, the number of radiosonde and ERA5 profiles used for the N-bias analysis is reduced to 396 and 319 profiles, respectively across the MAGIC transect.

3.1 PBL analysis

To evaluate the ducting properties along the transect from the coast of southern California to Hawaii, we group the MAGIC radiosonde and the colocated ERA5 profiles into eight 5˚ longitude

244 bins between −160.0˚ and −120.0˚, which allows for the assessment of the spatial variation of the

245 PBL, ducting layer, and the associated properties along the transect to be easily illustrated. Figure

246 4 shows the median value of PBLH (a), minimum gradient (b) and sharpness parameter (c) along

247 the transect. The median-absolute-deviation (MAD) for each parameter is also shown.

248 In Figure 4a, the MAGIC radiosondes (rds) clearly show a gradual increase of the PBLH along the

249 transect from the shallow stratocumulus-topped PBL (~800 m) near the southern California coast

250 westward to the much deeper trade-cumulus regime (~1.8 km) near Hawaii. A similar structure is

251 seen in the colocated ERA5 data but with an average low bias of 165 m below the radiosonde.

252 Additionally, a nearly 800 m ERA5 underestimation in PBLH over the two westernmost bins near

253 Hawaii is also seen, this is consistent with what is found over the equivalent trade cumulus region

254 of the subtropical southeast Pacific Ocean (Xie et al., 2012). Such a discrepancy could be due to

255 the sensitivity of the gradient method to the vertical resolution of the data. Over the western

256 segment of the transect (near Hawaii), two major gradient layers (one at ~1 km and the other at ~2

257 km) with comparable refractivity gradients are often observed (e.g., Fig. 2) in the ERA5 data. The

258 gradient layer near 2 km is well-known as the trade-wind inversion (Riehl, 1979; Ao et al., 2012;

259 Xie et al., 2012), while the lower-level gradient layer at ~1 km, is generally called a mixing layer

260 (Xie et al., 2006). Due to the differences in vertical sampling noted in Section 2.1, the ERA5 data

261 are more likely to resolve the sharp gradient structure below 1 km than the one at higher altitude.

262 This could result in resolving the mixing layer (below 1 km) with the sharpest refractivity gradient,

263 instead of the trade-wind inversion near 2 km in the ERA5 data. Note that the larger median

264 absolute deviation for the westernmost bins compared to the rest of the transect illustrates the

265 existence of greater PBLH variability closer to the trade-cumulus boundary layer regime. The

266 westward decreasing magnitude of the minimum refractivity gradient (Fig. 4b) and sharpness

267 parameter (Fig. 4c) indicates the westward weakening of moisture lapse rate and/or temperature

268 inversion across the PBL top, which is consistent with the decreasing synoptic-scale subsidence

269 from the California coast to Hawaii (Riehl, 1979).
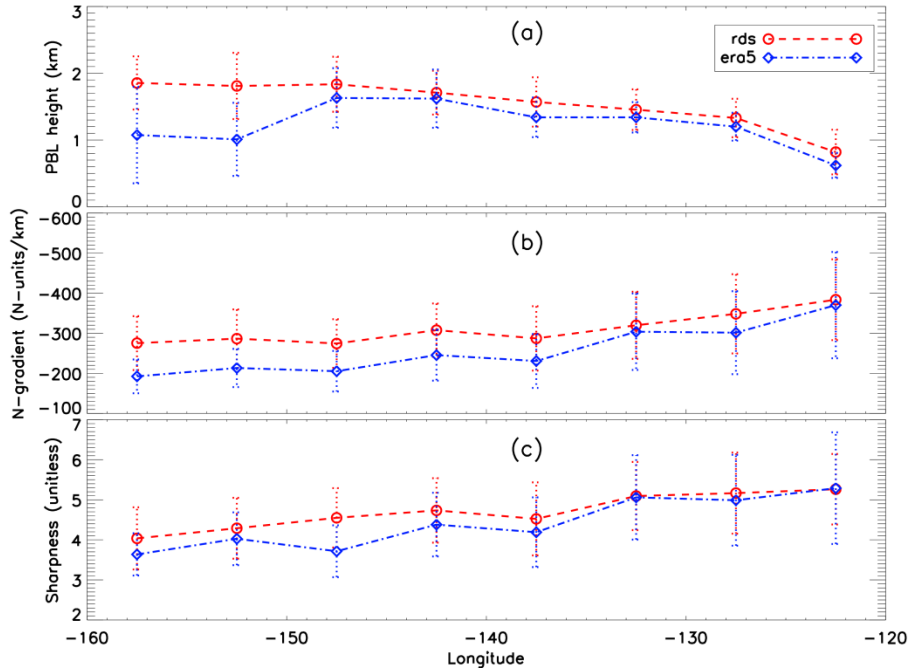
275   It is also notable that the ERA5 systematically underestimates not only the PBLH but also the

276   magnitude of the minimum gradient across the entire transect. This can also be seen in the

277   sharpness parameter west of $-132.5°$. This discrepancy could be partially attributed to the decrease

278   in vertical sampling in ERA5 profiles as compared to the radiosondes, the result of which leads to

279   a weaker PBL refractivity gradient and coincides with an increasing PBLH. Therefore, the

280   underestimation of the ERA5 minimum refractivity gradient increases in magnitude from east to

281   west and becomes most prominent near Hawaii where the PBLH reaches the maximum over the

282   region.

283   **3.2 Ducting characteristics**

284   As introduced in Sect. 2.3, the key characteristics of the ducting layer along the transect will be

285   investigated. These characteristics include the ducting layer height, ducting layer thickness (Δh),

286   and ducting strength (ΔN), as well as the average refractivity gradient within the ducting layer

287   ($\Delta N/\Delta h$). The ducting layer heights from both radiosondes and ERA5 show a westward increase

288   along the transect, as seen in Figure 5a. Note again that the ERA5 shows a systematic ~100–200

289   m low bias when compared to the radiosondes between $-122.5°$ and $-147.5°$, with the difference

11

290   increasing to more than 500 m near Hawaii. The ducting layer thickness is the median height from
291   the bottom of the ducting layer to the top and is expressed in km (Fig. 5b). Ducting thickness (Δh)
292   for MAGIC shows a near constant value of 110 m across the entire transect with only a slight
293   increase to 130 m at $-122.5°$, consistent with Ao et al. (2003). Conversely, the ERA5 shows a
294   constant but slightly thicker ducting layer to the east of $-137.5°$ and then a decreasing thickness to
295   the west of $-137.5°$ (Fig. 5b). It should be noted that the estimated thicknesses of the ducting
296   layers, especially for ERA5, may be affected by the chosen interpolation method.
297   The ducting layer strength is the decrease in refractivity from the bottom of the ducting layer to
298   the top (Fig. 5c) and the ratio $\Delta N/\Delta h$ reflects the average gradient of the ducting layer (Fig. 5d).
299   The ducting strength (ΔN) for the radiosondes generally ranges from 25 N-units near Hawaii to 40
300   N-units near the coast of California. Both ΔN and $\Delta N/\Delta h$ show an overall westward decreasing
301   trend along the transect which is consistent with the decrease in magnitude of the refractivity
302   gradient (Fig. 4b). Note that MAGIC and ERA5 show similar ducting strength in the eastern part
303   of the region but diverge near $-137.5°$ with ERA5 10 to 20 N-units weaker than the MAGIC
304   profiles. On the other hand, ERA5 shows a systematically lower average refractivity gradient
305   ($\Delta N/\Delta h$) than MAGIC throughout the transect, indicating the challenge in ERA5 to consistently
306   resolve the sharp vertical structure in refractivity, and likewise in temperature and moisture
307   profiles, across such a thin ducting layer. The problem becomes acutely clear near the trade
308   cumulus region.
309
310
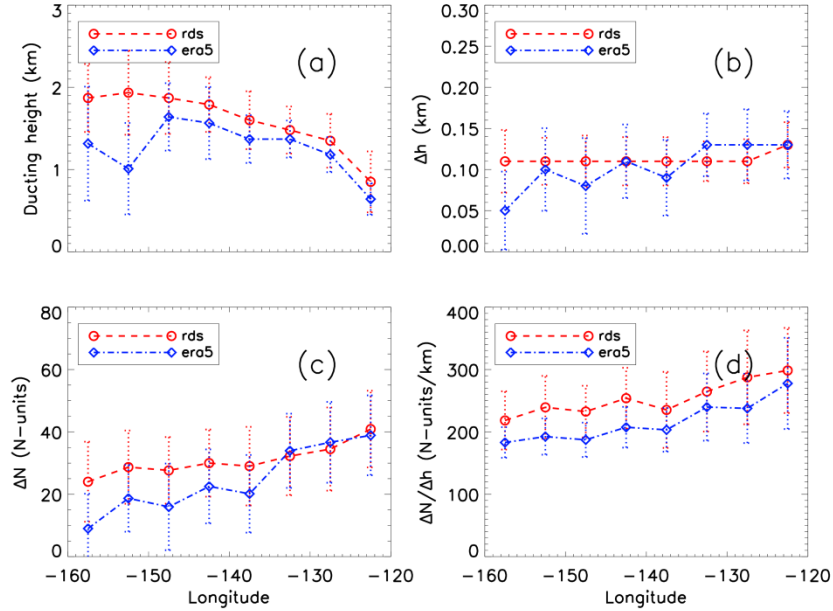
311
312 **Figure 5: Zonal transect of 5° binned median (a) ducting height, (b) ducting layer thickness (Δ***h***), (c) ducting layer strength**
313 **(Δ***N***), and (d) average ducting layer gradient Δ***N***/Δ***h*** for MAGIC (median in red circle and red-dashed line, MAD in red-**
314 **dotted error bars) and ERA5 (median in blue diamond and dot-dashed line, MAD in blue-dotted error bars).**
315

316 Figure 6 shows individual ducting layer thicknesses as a function of ducting layer strength. The

317 shape and color of each data point is used to identify its respective longitude bin. The relationship

318 between Δ*h* and Δ*N* is not longitude-dependent for either data set, but a linear trend is evident for

319 thinner ducting layers (Δ*h* < 0.1 km) with weaker ducting strength (Δ*N* < ~25 N-units). However,

320 for the ducting layers thicker than 0.1 km, such a trend becomes less identifiable, and the ducting

321 strength Δ*N* begins to show more variability toward larger values.

322
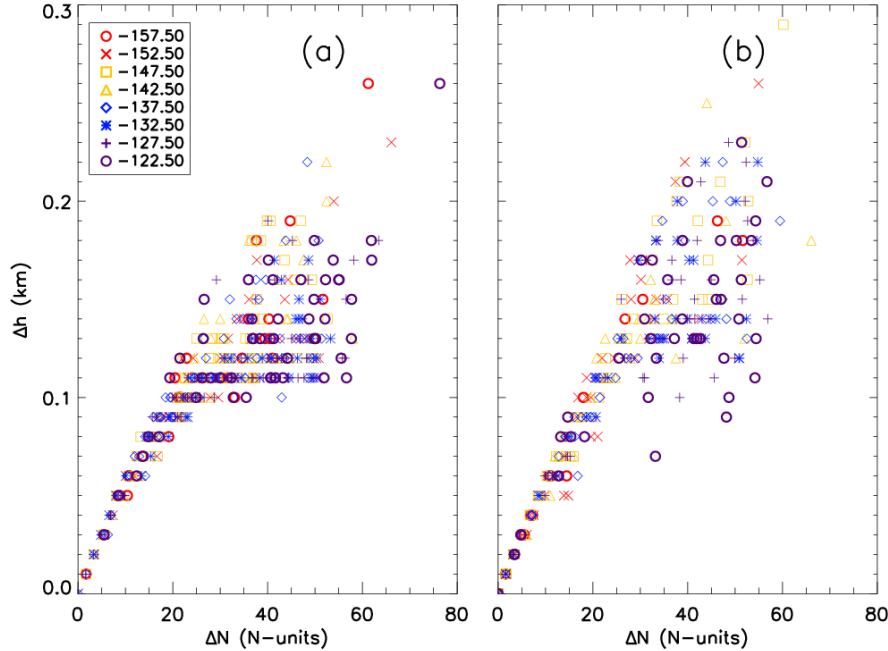
Figure 6: Comparison of individual profiles' ducting strength (ΔN) vs. ducting thickness (Δh) for MAGIC (a) and ERA5 (b). The shape and color of each character represents the location of the 5° longitude bin of each observation.

3.3 Ducting-induced GNSS RO *N*-bias statistics

To estimate the systematic negative *N*-bias in GNSS RO observations due to ducting, we have applied the end-to-end simulation described in Sect. 2.4 to all radiosonde and ERA5 refractivity profiles with at least one elevated ducting layer detected. The *N*-bias along the transect as well as its relationship to the ducting properties are presented below.

3.3.1 Assessing ducting-induced *N*-bias

Figure 7 shows a composite of both MAGIC (396 profiles) and ERA5 (319 profiles) *N*-bias profiles which have been displayed as a function of their zero-adjusted height. The median *N*-bias and MAD are also shown. The systematic negative *N*-bias peaks at approximately 100 m below the PBLH and decreases at lower relative altitudes. The peak median value of the *N*-bias for radiosondes is −5.42% (MAD, 2.92%), nearly twice the ERA5 value of −2.96% (MAD, 2.59%), indicating the significant underestimation of ducting strength in ERA5 data. However, the MAD of the radiosonde and ERA5 data are within 0.33% of each other, indicating that ERA5 data successfully capture the variations of ducting features seen in the radiosondes. It is worth noting that many radiosonde profiles show small negative *N*-biases above the PBLH (i.e., positive zero-

14

341 adjusted height), which is the result of a secondary ducting layer above the major ducting layer
342 near the PBLH. Few ERA5 profiles show the presence of the secondary ducting layer above PBLH.
343
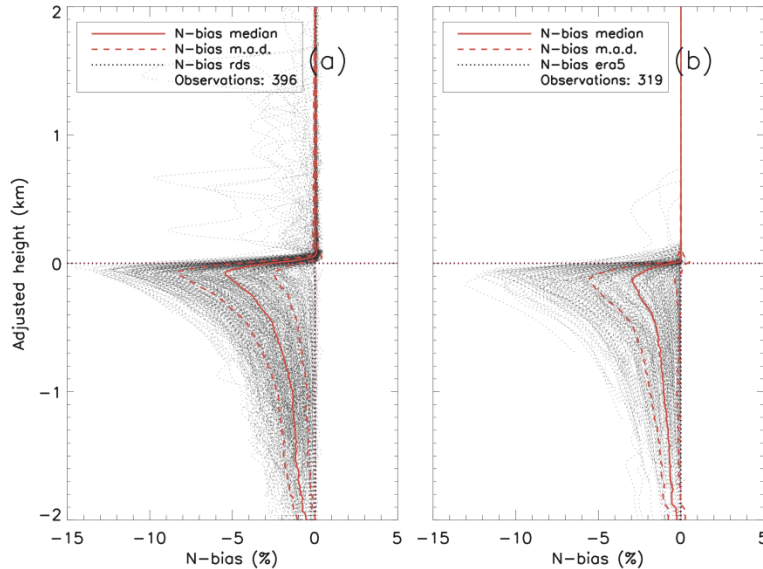
344
345 **Figure 7: Fractional refractivity difference (*N*-bias) between the simulated Abel-retrieved refractivity profile and the**
346 **original observed refractivity profile for all individual observations (dotted gray): (a) MAGIC radiosondes (396 total**
347 **profiles) and (b) ERA5 (319 total profiles) with population median (solid red) ± MAD (dashed red). Note the zero value in**
348 **the adjusted height refers to the detected PBLH for each individual *N*-bias profile.**

349 ### 3.3.2 Zonal variation of the *N*-bias along the transect

350 To illustrate the large variation in the *N*-bias vertical structure resulting from the spatial variations
351 of ducting height and strength, Figure 8 shows the median *N*-bias profiles (± MAD) for each 5°
352 bin, replacing the zero adjusted height with the median PBLH for each bin. The zonal radiosonde
353 composite (Fig. 8a) illustrates the westward transition of the median *N*-bias profiles from the
354 largest peak *N*-bias at ~0.8 km near the coast of Los Angeles, California, to a much-reduced peak
355 *N*-bias but higher altitude of ~1.8 km at Honolulu, Hawaii. Table 1 lists detailed statistics of the
356 peak *N*-bias values at each bin for both radiosonde and ERA5 data seen in Fig. 8. Although the
357 vertical structure of the *N*-bias profiles along the transect are consistent as seen in Fig. 7, significant
358 changes of the *N*-bias magnitude and its peak height along the transect are seen.
359 The maximum peak *N*-bias (−7.86%) in the radiosonde data is located at the easternmost of the
360 transect near California (−122.5°), whereas the minimum peak *N*-bias (−4.37%) is located near the
361 center of the transect (−147.5°). Similarly, the ERA5 also show the maximum peak *N*-bias
362 (−5.92%) near California (−122.5°). However, the minimum peak *N*-bias (−0.77%) is found near

Hawaii (−157.5˚). Overall, the *N*-bias values for the ERA5 data set are less than the *N*-bias values

calculated from the radiosonde data set for each longitude bin. However, a noticeable difference

exists between the ERA5 and radiosonde profiles for the two westernmost longitude bins (−157.5˚

and −152.5˚) where the ERA5 reveals a much lower and weaker *N*-bias than the MAGIC data.

The PBLH is above the height of the peak *N*-bias for both data sets. The MAGIC data show a

maximum difference of 100 m (−157.5˚) and a minimum difference of ~70 m (−142.5˚) while the

ERA5 PBLH shows greater values for maximum difference (140 m at −132.5˚) and minimum

difference (60 m at −157.5˚).
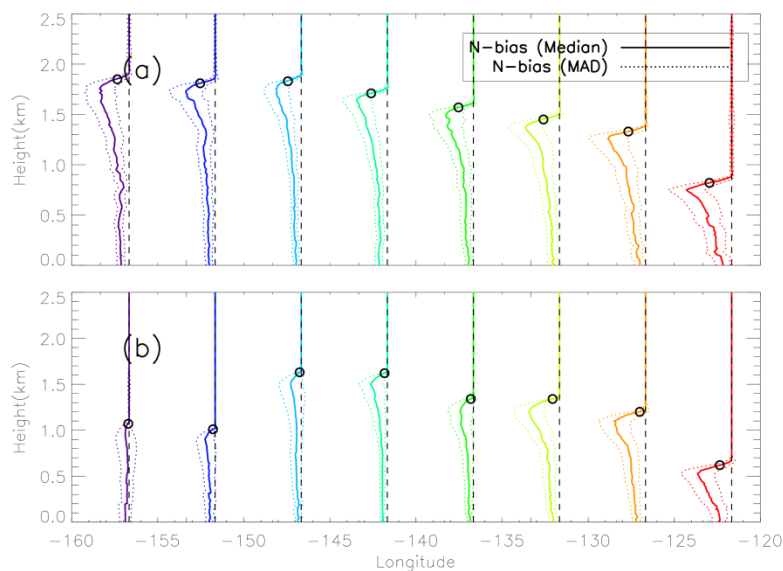
Figure 8: Median *N*-bias (solid) ± MAD (dotted) *N*-bias along the north Pacific transect for MAGIC radiosondes (a) and ERA5 (b). Open circles represent the median PBLH for each 5˚ bin. Vertical dashed line represents the location of each 5˚ grid bin. See Table 1 for corresponding values of median and M.A.D. peak *N*-bias.

Table 1: Peak values of median *N*-bias and corresponding MAD (%) values for MAGIC radiosondes (RDS) and ERA5 for each 5° bin seen in Figure 8.
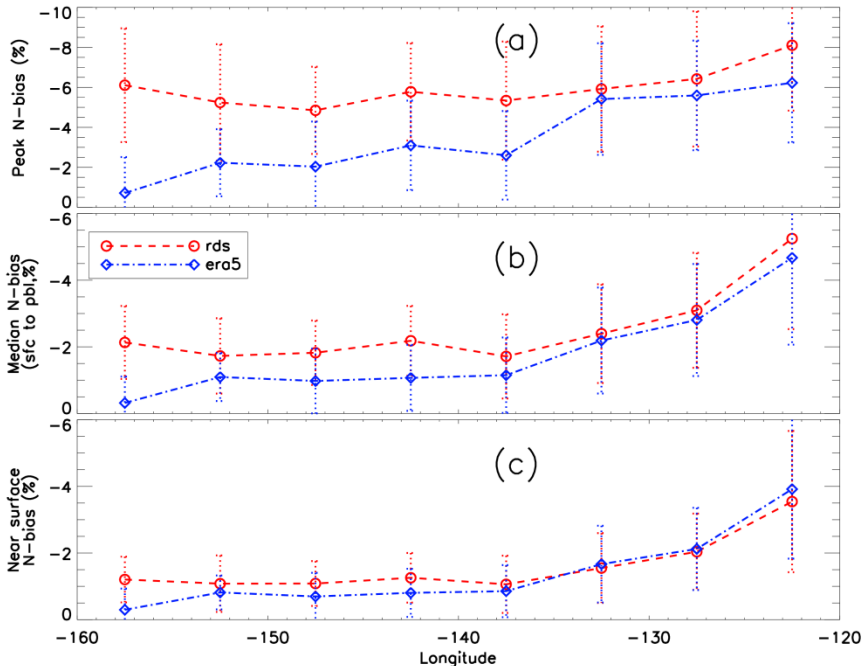
Peak N-bias (%)				
Longitude	RDS median	RDS MAD	ERA5 median	ERA5 MAD
−157.5°	−5.12	±2.61	−0.77	±1.73
−152.5°	−5.10	±2.97	−1.76	±1.61
−147.5°	−4.37	±2.14	−1.83	±2.10
−142.5°	−5.36	±2.53	−2.95	±2.17
−137.5°	−4.82	±2.96	−2.31	±2.14
−132.5°	−5.90	±3.03	−5.31	±2.68
−127.5°	−6.55	±3.40	−5.45	±2.88
−122.5°	−7.86	±3.15	−5.92	±3.04

Figure 9 further illustrates the peak *N*-bias, median PBL *N*-bias (0.3 km to PBLH), and the near surface *N*-bias (at 0.3 km) at each bin along the transect. Note the median PBL *N*-bias refers to the median value from the near-surface (0.3 km) to the PBLH. Contrary to the general trend of westward decrease in magnitude of the minimum refractivity gradient (Fig. 4b) and ducting strength (Fig. 5c), the radiosonde peak *N*-bias (median: −8.10%, MAD: 3.26%) occurs near California (−122.5°) and the minimum (median: −4.85%, MAD: 2.18%) occurs over the transition region (−147.5°). There is also a slight increase in peak *N*-bias to a secondary maximum (median: −6.11%, MAD: 2.85%) near Hawaii (−157.5°). The median PBL *N*-bias and the near surface *N*-bias also show a similar pattern. However, the median *N*-bias demonstrates a sharp decrease in the eastern half of the domain from −5.25% (MAD: 2.71%) at −122.5° to −1.71% (MAD: 1.26%) at −137.5°, and then remains relatively constant over the western half of the domain. Similarly, the near surface *N*-bias reaches a maximum magnitude of −3.54% (MAD: 2.11%), sharply decreases to −1.06% (MAD: 0.85%) at −137.5°, and then remains relatively constant over the western half of the domain. Note that normalizing each *N*-bias profile to the PBLH preserves the magnitude of the *N*-bias with various heights. Therefore, the relatively large, normalized *N*-biases observed near Hawaii indicates more persistent ducting over the trade-cumulus boundary layer regime compared to the transition region in the middle of the transect at -147.5° (Fig. 8a).

On the other hand, the ERA5 data show a westward decrease of all three *N*-biases, systematically underestimating all three as compared to the radiosondes. This is expected as the decrease of ERA5 vertical resolution at higher altitude leads to a weaker PBL *N*-gradient observation (Fig. 4b), and thus weaker ducting and a smaller ducting-induced *N*-bias. Such underestimation of the *N*-bias in the ERA5 reanalysis minimizes near California where the PBLH is lowest but becomes more

severe westward with an increase in height, reaching a maximum magnitude *N*-bias difference

near Hawaii. In this case, the peak *N*-bias is merely −0.71% (MAD: 1.80%) as compared to −6.23%

(MAD: 2.98%) at −122.5˚ (Fig. 9a). The large difference seen in the *N*-bias along the transect

strongly indicates the challenges of the ERA5 data to resolve the sharp gradient across the ducting

layer, resulting in a large variation in PBLH of the ERA5 data in the western segment of the region.

The increasing difference between the radiosonde and ERA5 data from east to west is most

pronounced in the peak *N*-bias cross-section (Fig. 9a) but is also evident in both the median *N*-bias

(Fig. 9b) as well as the near surface *N*-bias (Fig. 9c).

Figure 9: Zonal transect of 5˚ binned (a) peak *N*-bias, (b) median PBL *N*-bias (0.3 km to PBLH), and (c) near surface *N*-bias at 0.3 km for MAGIC (median in red circle and red-dashed line, MAD in red-dotted error bar) and ERA5 (median in blue diamond and dot-dashed line, MAD in blue-dotted error bar)

4   Summary and Conclusions

In this study, radiosonde profiles from the MAGIC field campaign have been analyzed to

investigate ducting characteristics and the induced systematic refractivity biases in GNSS RO

retrievals over the Northeastern Pacific Ocean between Hawaii and California. Colocated ERA5

model reanalysis data were used as a secondary comparison to the radiosonde observations.

The nearly 1-year high-resolution MAGIC radiosonde data set reveals the frequent presence of

ducting marked by a sharp refractivity gradient resulting from the large moisture lapse rate across

a strong temperature inversion layer. The PBLH increases by more than 1 km along the transect

442 from California to Hawaii, while the magnitude of the refractivity gradient decreases by 100 N-

443 units km^{-1}. The zonal gradient of both variables illustrates the transition of the PBL from shallow

444 stratocumulus adjacent to the California coast to deeper trade-wind cumulus that are prevalent near

445 the Hawaiian Islands.

446 End-to-end simulations on all radiosonde and ERA5 refractivity profiles have been conducted to

447 estimate the systematic negative N-bias in GNSS RO observations. The ducting layer maintains

448 remarkably consistent thickness (~110 m) along the transect with westward decreasing strength

449 and increasing height. The ERA5 slightly underestimates both the height and strength of the

450 ducting layer as well as the PBLH. A systematic negative N-bias below the ducting layer is

451 observed throughout the transect, peaking (−5.42%) slightly below the PBLH, and gradually

452 decreasing towards the surface (−0.5%).

453 MAGIC radiosondes indicate larger values of both ducting strength (ΔN) and thickness (Δh) than

454 ERA5 in the western half of the transect. The opposite is true in the eastern portion of the domain

455 and is likely associated with the transition of the cloud layer from open-cell cumulus in the west

456 to stratocumulus and stratus in the east (Wood et al., 2011; Bretherton et al., 2019). ERA5

457 systematically underestimates the average ducting layer gradient ($\Delta N/\Delta h$) comparing to the

458 radiosondes. The largest N-bias is found over the region with strongest ducting and largest

459 sharpness parameter. It is worth noting that the PBL over the western portion of the transect near

460 Hawaii frequently shows two major gradient layers (a mixing layer at ~1 km and the trade-

461 inversion at ~2 km), with comparable N-gradients (e.g., Fig. 2). The much lower PBLH seen in

462 ERA5 in this region is likely due, in part, to the decreasing number of model levels in ERA5 at

463 higher altitude, which could lead to a higher possibility of identifying the lower gradient layer as

464 the PBLH. However, the impact of the vertical resolution and on the performance of the gradient

465 method for PBLH detection has not been performed in this study. Further, the ERA5 results may

466 be affected by the interpolation resolution and gradient are calculation. Both warrant a more

467 comprehensive study in the future.

468 **5   Data availability**

469 Data for the Marine Atmospheric Radiation Measurement (ARM) GCSS Pacific Cross Section

470 Intercomparison (GPCI) Investigation of Clouds (MAGIC, Zhou et al., 2015) can be accessed

471 through the U.S. Department of Energy's Office of Science
472 https://www.arm.gov/research/campaigns/amf2012magic.
473 Data for the ECMWF Reanalysis version 5 (ERA5, Hersbach et al., 2020) can be accessed at
474 https://www.ecmwf.int/en/forecasts/dataset/ecmwf-reanalysis-v5.

6   Author contribution

Author Thomas Winning is responsible for all original text data analysis, and production of graphics. Author Kevin Nelson contributed by providing updated data processing and end-to-end simulation code, colocation of ERA5 data with MAGIC observations, and manuscript edits. Author Feiqin Xie is the academic advisor for the primary author and also provided draft edits and paper organization and writing guidance.

7   Competing interests

The authors declare no competing interests, see Acknowledgements for current affiliations.

8   Acknowledgements

498 **References**

499 Anthes, R. A., and Coauthors: The COSMIC/FORMOSAT-3 Mission: Early Results, BAMS, 89, 313–334,
500 doi.org/10.1175/bams-89-3-313, 2008.
501
502 Ao, C. O., Meehan T. K., Hajj, G. A., Mannucci, A. J., and Beyerle, G.: Lower Troposphere Refractivity Bias in GPS
503 Occultation Retrievals, J. Geophys. Res., 108, 4577, doi:10.1029/2002JD003216, 2003.
504
505 Ao, C. O.: Effect of Ducting on Radio Occultation Measurements: An Assessment Based on High-resolution
506 Radiosonde Soundings, Radio Sci., 42, RS2008, doi.org/10.1029/2006RS003485, 2007.
507
508 Ao, C. O., Chan, T. K., Iijima, A., Li, J.-L., Mannucci, A. J., Teixeira, J., Tian, B., and Waliser, D. E.: Planetary
509 Boundary Layer Information from GPS Radio Occultation Measurements, in: Proceedings of the GRAS SAF
510 Workshop on Applications of GPSRO Measurements, Vol. 5 of, GRAS SAF Workshop on Applications of GPSRO
511 Measurements,   Reading,   United   Kingdom,   ECMWF   and   EUMETSAT,   123–131,
512 https://www.ecmwf.int/sites/default/files/elibrary/2008/7459-planetary-boundary-layer-information-gps-radio-
513 occultation-measurements.pdf, 16–18 June, 2008.
514
515 Ao, C. O., Waliser, D. E., Chan, S. K., Li, J.-L., Tian, B., Xie, F., and Mannucci, A. J.: Planetary boundary layer
516 heights from GPS radio occultation refractivity and humidity profiles, J. Geophys. Res., 117, D16117,
517 doi:10.1029/2012JD017598, 2012.
518
519 Basha, G., and Ratnam, M. V.: Identification of atmospheric boundary layer height over a tropical station using high-
520 resolution radiosonde refractivity profiles: Comparison with GPS radio occultation measurements, J. Geophys. Res.,
521 114, doi.org/10.1029/2008jd011692, 2009.
522
523 Beyerle, G., Gorbunov, M. E., and Ao, C.O.: Simulation studies of GPS radio occultation measurements, Radio Sci.,
524 38, 1084, doi:10.1029/2002RS002800, 2003.
525
526 Bretherton, C.S., and Coauthors: Cloud, Aerosol, and Boundary Layer Structure across the Northeast Pacific
527 Stratocumulus–Cumulus Transition as Observed during CSET, Mon.Wea. Rev., 147, 2083–2102. DOI:
528 10.1175/MWR-D-18-0281, 2019
529
530 Eshleman, V.R.: The radio occultation method for the study of planetary atmospheres, Planet. Space Sci., 21, 1521-
531 1531, doi.org/10.1016/0032-0633(73)90059-7, 1973.
532

533 Feng, X., Xie, F., Ao, C.O., and Anthes, R.A.: Ducting and Biases of GPS Radio Occultation Bending Angle and
534 Refractivity in the Moist Lower Troposphere, J. Atmos. Oceanic Technol., 37, 1013–1025, doi.org/10.1175/JTECH-
535 D-19-0206.1, 2020.

536

537 Fjeldbo, G., and Eshleman, V.R.: The Atmosphere of Mars Analyzed by Integral Inversion of the Mariner IV
538 Occultation Data, Planet. Space Sci., 16, 1035-1059, doi.org/10.1016/0032-0633(68)90020-2, 1968.

539

540 Fjeldbo, G., Kliore, A.J., and Eshleman, V.R.: The Neutral Atmosphere of Venus as Studied with the Mariner V Radio
541 Occultation Experiment, Astron. J., 76, 123-140, doi.org/10.1086/111096, 1971.

542

543 Garratt, J. R.: Review: the atmospheric boundary layer, Earth-Sci. Rev., 37, 89–134, 1994

544

545 Guo, P., Kuo, Y. H., Sokolovskiy, S. V., and Lenschow, D. H.: Estimating Atmospheric Boundary Layer Depth Using
546 COSMIC Radio Occultation Data, J. Atmos. Sci., 68, 1703–1713, doi.org/10.1175/2011jas3612.1, 2011.

547

548 Gorbunov, M. E.: Canonical transform method for processing radio occultation data in the lower troposphere, Radio
549 Sci., 37(5), 1076, doi:10.1029/2000RS002592, 2002.

550
551 Gorbunov, M. E., Benzon, H. H., Jensen, A.S, Lohmann, M.S., and Nielsen, A.S.: Comparative analysis of radio
552 occultation processing approaches based on Fourier integral operators. Radio Sci., 39, RS6004,
553 https://doi.org/10.1029/2003RS002916, 2004

554

555 Healy, S. B.: Radio occultation bending angle and impact parameter errors caused by horizontal refractive index
556 gradients in the troposphere: A simulation study, J. Geophys. Res, 106, D11, 11875–11889,
557 doi:10.1029/2001JD900050, 2001.

558

559 Hersbach, H., Bell, B., Berrisford, P., Hirahara, S., Horányi, A., Muñoz-Sabater, J., Nicolas, J., Peubey, C., Radu, R.,
560 Schepers, D., Simmons, A., Soci, C., Abdalla, S., Abellan, X., Balsamo, G., Bechtold, P., Biavati, G., Bidlot, J.,
561 Bonavita, M., De Chiara, G., Dahlgren, P., Dee, D., Diamantakis, M., Dragani, R., Flemming, J., Forbes, R., Fuentes,
562 M., Geer, A., Haimberger, L., Healy, S., Hogan, R. J., Hólm, E., Janisková, M., Keeley, S.,
563 Laloyaux, P., Lopez, P., Lupu, C., Radnoti, G., de Rosnay, P., Rozum, I., Vamborg, F., Villaume, S., and Thépaut, J.-
564 N.: The ERA5 Global Reanalysis, Q. J. Roy. Meteor. Soc., 146, 1999–2049, https://doi.org/10.1002/qj.3803, 2020.

565
566 Ho, S.-P., Peng, L., Anthes, R. A., Kuo, Y.-H., and Lin, H.-C.: Marine boundary layer heights and their longitudinal,
567 diurnal and inter-seasonal variability in the southeast Pacific using COSMIC, CALIOP, and radiosonde data. J.
568 Climate, 28, 2856–2872, https://doi.org/10.1175/JCLI-D-14-00238.1, 2015.

569

570   Jensen, A. S., Lohmann, M.S., Nielsen, A.S. and Benzon, H.-H.: Geometrical optics phase matching of radio

571   occultation signals, Radio Sci., 39, RS3009, doi:10.1029/2003RS002899, 2004.

572

573   Jensen, A. S., Lohmann, M.S., Benzon, H.-H, and Nielsen, A.S.: Full spectrum inversion of radio occultation signals,

574   Radio Sci., 38(3), 1040, doi:10.1029/2002RS002763, 2003.

575

576   Johnston, B. R., Xie, F., and Liu, C.: The effects of deep convection on regional temperature structure in the tropical

577   upper troposphere and lower stratosphere, J. Geophys. Res.: Atmos., 123, 1585−1603,

578   doi.org/10.1002/2017JD027120, 2018.

579

580   Klein, S. A., and Hartmann, D. L.: The seasonal cycle of low stratiform clouds. Journal of Climate, 6, 1587−1606,

581   doi:10.1175/1520-0442(1993)006<1587:TSCOLS>2.0.CO;2, 1993.

582

583   Kursinski, E. R., Hajj, G. A., Schofield, J. T., Linfield, R. P., and Hardy, K. R.: Observing Earth's atmosphere with

584   radio occultation measurements using the Global Positioning System, J. Geophys. Res.: Atmos., 102, 23429−23465,

585   doi.org/10.1029/97jd01569, 1997.

586

587   Kursinski, E. R., G. A. Hajj, Leroy, S. S., and Herman, B.: The GPS Radio Occultation Technique. Terr. Atmos.

588   Ocean. Sci. (TAO), 11, 53−114, 2000.

589

590   Lewis, E. R.: Marine ARM GPCI Investigation of Clouds (MAGIC) Field Campaign Report. U.S. Department of

591   Energy, https://doi.org/10.2172/1343577, 2016.

592

593   Maddy, E. S. and Barnet, C. D.: Vertical resolution estimates in version 5 of AIRS operational retrievals. IEEE

594   Transactions on Geoscience and Remote Sensing, 46, 2375−2384, doi:10.1109/TGRS.2008.917498, 2008.

595

596   Nelson, K. J., Xie, F., Ao, C. O., and Oyola-Merced, M. I.: Diurnal Variation of the Planetary Boundary Layer Height

597   Observed from GNSS Radio Occultation and Radiosonde Soundings over the Southern Great Plains. J. Atmos.

598   Oceanic Tech., 38, 2081−2093, https://doi.org/10.1175/jtech-d-20-0196.1, 2021.

599

600   Nelson, K. J., Xie, F., Chan, B. C., Goel, A., Kosh, J., Reid, T. G. R., Snyder, C. R., and Tarantino, P. M.: GNSS

601   Radio Occultation Soundings from Commercial Off-the-Shelf Receivers Onboard Balloon Platforms, Atmos. Meas.

602   Tech., https://doi.org/10.5194/amt-2022-198, 2022.

603

604   Painemal, D., Minnis, P., and Nordeen, M.: Aerosol variability, synoptic-scale processes, and their link to the cloud

605   microphysics over the northeast Pacific during MAGIC, J. Geophys. Res. Atmos., 120, 5122–5139,

606   doi:10.1002/2015JD023175, 2015.

607

608 Patterson, W. L.: Climatology of Marine Atmospheric Refractive Effects: A Compendium of the Integrated Refractive

609 Effects   Prediction   System   (IREPS)   Historical   Summaries.   Naval   Ocean   Systems   Center,

610 https://apps.dtic.mil/sti/pdfs/ADA155241.pdf, 1982.

611

612 Ramanathan, V., Cess, R. D., Harrison, E. F., Minnis, P., Barkstrom, B. R., Ahmad, E., and Hartmann, D.: Cloud-

613 radiative forcing and climate: Results from the Earth Radiation Budget Experiment, Science, 243, 57–63,

614 DOI:10.1126/science.243.4887.57, 1989.

615

616 Riehl, H.: Climate and weather in the tropics. London: Academic Press. 611 pp. ISBN 0.12.588180.0

617

618 Rocken, C., Anthes, R., Exner, M., Hunt, D., Sokolovskiy, S., Ware, R., Gorbunov, M., Schreiner, W., Feng

619 D., Herman B., Kuo, Y.-H., Zou, X.: Analysis and validation of GPS/MET data in the neutral atmosphere. J. Geophys.

620 Res., 102, 29849−29866, https://doi.org/10.1029/97JD02400, 1997.

621

622 Schreiner, W. S., Weiss, J.P., Anthes, R.A., Braun, J., Chu, V., Fong, J., Hunt, D., Kuo, Y.-H., Meehan, T., Serafino,

623 W., Sjoberg, J., Sokolovskiy, C., Talaat, E., Wee, T.K., Zeng, Z.: COSMIC-2 Radio Occultation Constellation: First

624 Results. Geophys. Res. Lett., 47, https://doi.org/10.1029/2019gl086841, 2020.

625

626 Seidel, D. J., Ao, C.O. and Li, K.: Estimating climatological planetary boundary layer heights from radiosonde

627 observations: Comparison   of   methods   and   uncertainty   analysis,   J.   Geophys.   Res.,   115,   D16114,

628 doi:10.1029/2009JD013680, 2010.

629

630 Smith, E. K. and Weintraub, S.: The Constants in the Equation for Atmospheric Refractivity Index at Radio

631 Frequencies. Proc. IRE, 41, 1035−1037, doi:10.1109/JRPROC.1953.274297, 1953.

632

633 Sokolovskiy, S. V.: Modeling and Inverting Radio Occultation Signals in the Moist Troposphere. Radio Sci., 36,

634 441−458, https://doi.org/10.1029/1999RS002273, 2001.

635

636 Sokolovskiy, S. V.: Effect of super refraction on inversions of radio occultation signals in the lower troposphere.

637 Radio Sci., 38 (3), https://doi.org/10.1029/2002RS002728, 2003.

638

639 Sokolovskiy, S. V., Kuo, Y.-H., Rocken, C., Schreiner, W. S., Hunt, D. and Anthes, R. A., 2006: Monitoring the

640 atmospheric boundary layer by GPS radio occultation signals recorded in the open-loop mode. Geophys. Res. Lett.,

641 33, L12813, doi:10.1029/2006GL025955, 2006.

642

643 Stull, R., Santoso, E., Berg, L. K., and Hacker, J.: Boundary Layer Experiment 1996 (BLX96), BAMS, 78,
644 1149−1158, doi: 10.1175/1520-0477(1997)078<1149:BLEB>2.0.CO;2, 1997.

646 Stull, R. B.: An Introduction to Boundary Layer Meteorology. Kluwer Academic Publishers, 666 pp., ISBN 90-277-
647 2768-6, 1988.

649 von Engeln, A. and Teixeira, J.: A Planetary Boundary Layer Height Climatology Derived from ECMWF Reanalysis
650 Data, J. Climate, 26, 6575−6590, https://doi.org/10.1175/jcli-d-12-00385.1, 2013.

652 Winning, T. E., Chen, Y.-L., and Xie, F.: Estimation of the marine boundary layer height over the central North Pacific
653 using GPS radio occultation, Atmospheric Research, 183, 362−370, https://doi.org/10.1016/j.atmosres.2016.08.005,
654 2017.

656 Wood, R., Mechoso, C. R., Bretherton, C. S., Weller, R. A., Huebert, B., Straneo, F., Albrecht, B. A., Coe, H., Allen,
657 G., Vaughan, G., Daum, P., Fairall, C., Chand, D., Gallardo Klenner, L., Garreaud, R., Grados, C., Covert, D. S.,
658 Bates, T. S., Krejci, R., Russell, L. M., de Szoeke, S., Brewer, A., Yuter, S. E., Springston, S. R., Chaigneau, A.,
659 Toniazzo, T., Minnis, P., Palikonda, R., Abel, S. J., Brown, W. O. J., Williams, S., Fochesatto, J., Brioude, J., and
660 Bower, K. N.: The VAMOS Ocean-Cloud-Atmosphere-Land Study Regional Experiment (VOCALS-REx): goals,
661 platforms, and field operations, Atmos. Chem. Phys., 11, 627−654, https://doi.org/10.5194/acp-11-627-2011, 2011.

663 Xie, F., Syndergaard, S., Kursinski, E. R., and Herman, B.M.: An Approach for Retrieving Marine Boundary Layer
664 Refractivity from GPS Occultation Data in the Presence of Super-refraction. J. Atmos. Oceanic Technol., 23,
665 1629−1644, https://doi.org/10.1175/JTECH1996.1, 2006.

667 Xie, F., Haase, J. S., and Syndergaard, S.: Profiling the Atmosphere Using the Airborne GPS Radio Occultation
668 Technique: A Sensitivity Study. IEEE Transactions on Geoscience and Remote Sensing, 46, 3424−3435,
669 https://doi.org/10.1109/tgrs.2008.2004713, 2008.

671 Xie, F., Wu, D. L., Ao, C. O., Kursinski, E. R., Mannucci, A. J., and Syndergaard, S.: Super-refraction effects on GPS
672 radio occultation refractivity in marine boundary layers, Geophys. Res. Lett., 37,
673 https://doi.org/10.1029/2010gl043299, 2010.

675 Xie, F., Wu, D. L., Ao, C. O., Mannucci, A. J., and Kursinski, E. R.: Advances and limitations of atmospheric boundary
676 layer observations with GPS occultation over southeast Pacific Ocean, Atmos. Chem. Phys., 12, 903−918,
677 doi:10.5194/acp-12-903-2012, 2012.

679 Zhou, X., Kollias, P., and Lewis, E.: Clouds, precipitation and marine boundary layer structure during MAGIC. J.
680 Climate, 28, 2420−2442, https://doi.org/10.1175/JCLI-D-14-00320.1, 2015.